



Effect of Ni/Fe/Mn ratio on electrochemical properties of the O3-NaNi_{1-x-y}Fe_xMn_yO₂ (0.25 ≤ x,y ≤ 0.75) cathode materials for Na-ion batteries

Vitalii A. Shevchenko^{a,b}, Alena I. Komayko^b, Elizaveta V. Sivenkova^a, Ruslan R. Samigullin^a, Irina A. Skvortsova^b, Artem M. Abakumov^b, Viktoria A. Nikitina^b, Oleg A. Drozhzhin^{a,*}, Evgeny V. Antipov^{a,b}

^a Department of Chemistry, Lomonosov Moscow State University, 119991, Moscow, Russian Federation

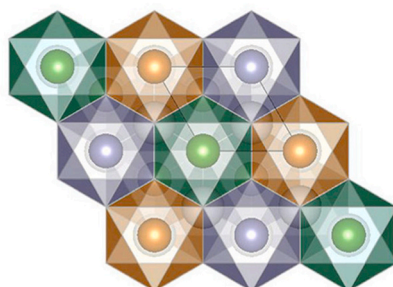
^b Center for Energy Science and Technology, Skolkovo Institute of Science and Technology, Nobel St. 3, 143026, Moscow, Russian Federation

HIGHLIGHTS

- Influence of the Fe/Mn/Ni ratio on the electrochemical properties of NaMO₂ is studied.
- Equimolar and Mn-rich samples demonstrate the best cycling and thermal stability.
- Equimolar NaNi_{1/3}Fe_{1/3}Mn_{1/3}O₂ sample exhibits the highest diffusion coefficients.
- Equimolar and Mn-rich samples demonstrate the lowest growth in R_{ct} upon cycling.
- Equimolar oxide retain up to 80 % of the capacity upon cooling down to -30 °C.

GRAPHICAL ABSTRACT

Effect of Ni/Fe/Mn ratio in O3-NaMO₂ on:



- Phase composition
- Capacity & cycling stability
- Diffusion & kinetics
- Low-temperature performance
- Thermal stability

ABSTRACT

Layered O3-type NaMO₂ oxides (M = transition metals) are the main candidates for cathode materials in the actively developing technology of sodium-ion batteries. Nevertheless, despite many years of research, the optimal composition of such materials is still a matter of debate. In this work, we studied the effect of the Fe, Mn and Ni content on the phase composition, structure, thermal stability and electrochemical properties of the cathode materials NaNi_{1/3}Fe_{1/3}Mn_{1/3}O₂ (NFM111), NaNi_{0.5}Fe_{0.25}Mn_{0.25}O₂ (NFM211), NaNi_{0.25}Fe_{0.5}Mn_{0.25}O₂ (NFM121) and NaNi_{0.25}Fe_{0.25}Mn_{0.5}O₂ (NFM112). All materials demonstrate similar discharge capacity (125–131 mAh·g⁻¹) when cycling in the 1.9–4.0 V vs Na/Na⁺ potential range. However, only the NFM111 and NFM112 samples show a low increase in charge transfer resistance during cycling and acceptable thermal stability. Low-temperature experiments revealed good capacity retention for the NFM111 electrode material with loss of only ~20 % of capacity when the temperature drops from +25 to -30 °C. Thus, the NFM111 oxide exhibits a balanced combination of the electrochemical properties and, along with manganese-enriched composition, can be considered as a good choice for further development of cathode materials for sodium-ion batteries.

* Corresponding author.

E-mail address: drozhzhin@elch.chem.msu.ru (O.A. Drozhzhin).

<https://doi.org/10.1016/j.jpowsour.2024.234092>

Received 7 October 2023; Received in revised form 12 December 2023; Accepted 12 January 2024

0378-7753/© 2024 Elsevier B.V. All rights reserved.

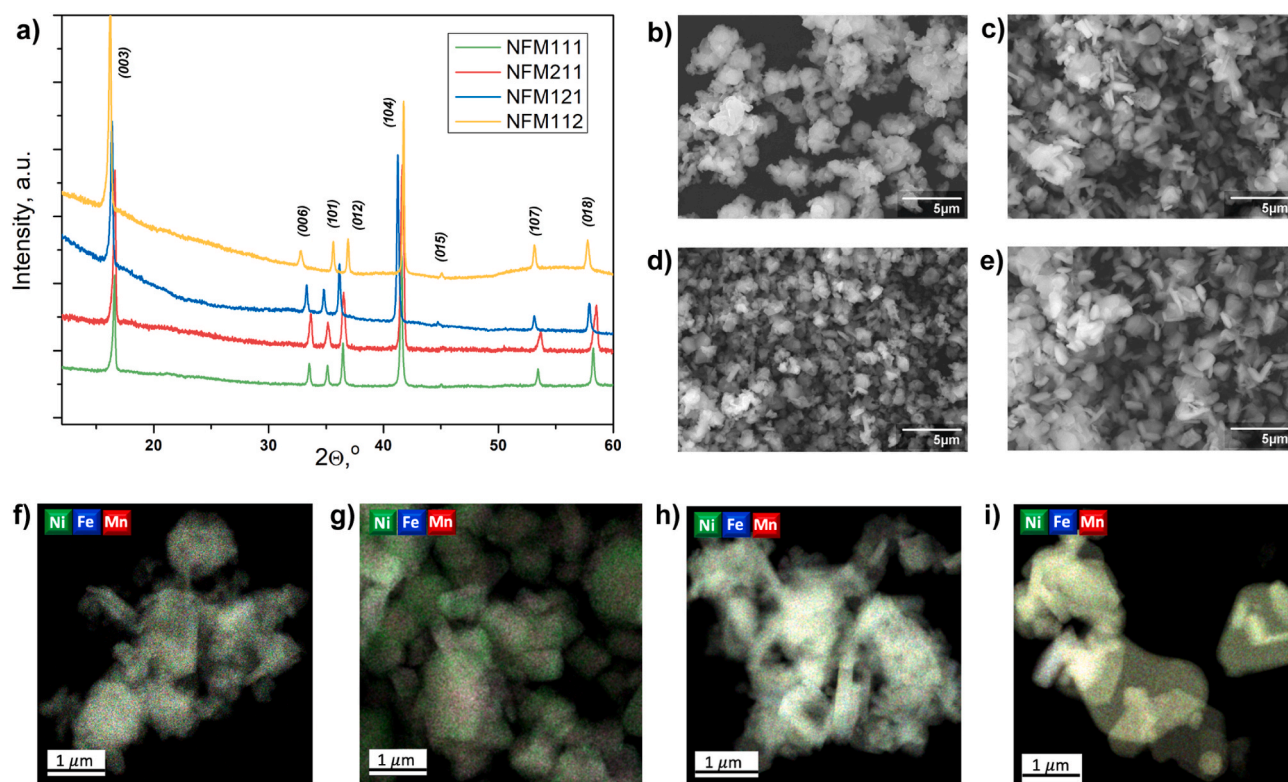


Fig. 1. PXRD patterns (a), SEM images (b–e) and mixed EDX maps (f–i) for the NFM111 (b,f), NFM211 (c,g), NFM121 (d,h) and NFM112 (e,i) samples. Indices shown in Fig. 1a correspond to the $R\bar{3}m$ structure.

Table 1
Unit cell parameters of the samples.

Sample	a , Å	b , Å	c , Å	α , deg.	β , deg.	γ , deg.	V , Å ³
O3–NaNi _{1/3} Fe _{1/3} Mn _{1/3} O ₂ (NFM 111), sp. gr. $R\bar{3}m$,	2.9825(1)	–	15.999(2)	90	90	120	123.25(1)
O ³ –NaNi _{0.5} Fe _{0.25} Mn _{0.25} O ₂ (NFM 211), sp. gr. $C2/m$	5.1382(6)	2.9820(5)	5.5801(2)	90	107.87(1)	90	81.37(5)
O3–NaNi _{0.25} Fe _{0.5} Mn _{0.25} O ₂ (NFM 121), sp. gr. $R\bar{3}m$	2.9900(1)	–	16.041(1)	90	90	120	124.19(3)
O3–Na _{0.71} Ni _{0.25} Fe _{0.25} Mn _{0.5} O ₂ (NFM 112) ^a , sp. gr. $R\bar{3}m$	2.9390(2)	–	16.346(1)	90	90	120	122.27(8)
O3–NaNi _{0.25} Fe _{0.25} Mn _{0.5} O ₂ (NFM 112) electrode discharged to 1.9 V, sp. gr. $R\bar{3}m$	2.9691(1)	–	16.108(9)	90	90	120	122.98(3)

^a Na content is determined by means of Rietveld refinement.

1. Introduction

Sodium-ion batteries (SIBs) is a technology that has many hopes due to the mismatch between the human need for efficient and inexpensive solutions for energy storage, on the one hand, and the high cost and inaccessibility of lithium resources, on the other [1–3]. As in the case of the “parental” technology of lithium-ion batteries (LIBs), the key components of SIBs are electrode materials. Particularly, positive electrode (cathode) is the main element that determines the energy density, power, cyclability and safety of the battery. Search and optimization of the cathode materials is carried out within several types of chemical compounds: layered transition metal and sodium oxides, polyanion materials such as phosphates, pyrophosphates, fluoride phosphates etc., and organic/polymer compounds [4]. Among them, oxides exhibit the highest energy density being considered as the main candidates for commercial deployment [1–4].

In contrast to LIBs, in which LiCoO₂ cathode material is still used commercially, in SIBs the NaMO₂ cathodes with a single d-cation M appear impractical due to structural distortions, cation migration and resulting voltage hysteresis during Na⁺ (de)intercalation occurring because of Jahn-Teller effect for Fe⁴⁺, Mn³⁺ and Ni³⁺ cations [5–10]. For Na(M1_{1-x}M2_x)O₂ these effects are significantly depressed, whereas ternary compositions demonstrate quite smooth charge-discharge

curves with low overvoltage and attractive cycling stability. For example, it was shown that Ni and Mn co-substitution of Fe in O3–NaFeO₂ effectively prevents migration of iron and suppresses capacity fading. So, NaFe_{0.4}(Ni_{1/2}Mn_{1/2})_{0.6}O₂, as the solid solution of Na(Ni_{1/2}Mn_{1/2})O₂ and NaFeO₂, can deliver 130 mAh g⁻¹ of reversible capacity in a voltage range of 2.0–3.8 V vs. Na/Na⁺, yet it shows very smooth charge/discharge curves with no significant voltage hysteresis [11]. Optimizing ratio of Fe and Ni with the fixed Mn content of 25 % in Na[Ni_{0.75-x}Fe_xMn_{0.25}]O₂ (x = 0.4, 0.45, 0.5 and 0.55) revealed a positive effect of increasing the amount of nickel on capacity and a negative - on cycling and thermal stability [12].

Further rising the number of d-cations, e.g. up to 9 in so-called “high entropy” systems does not seem to be reasonable, as it complicates the synthesis of the materials with homogeneous distribution of so many d-cations in the crystal structure [13]. In this regard, ternary systems appear as a reasonable compromise between stable and attractive electrochemical properties, on the one hand, and simplicity and reproducibility of the synthesis, on the other. O3–NaNi_{1/3}Fe_{1/3}Mn_{1/3}O₂ is the most studied within this family. It demonstrates the capacity of ≈130 mAh·g⁻¹ and stable cycling when upper potential cutoff is limited to 4.0 V vs. Na/Na⁺. With an increase in this value to 4.2–4.3 V, the reversible capacity increases to ≈160 mAh·g⁻¹ due to the presence of a high voltage plateau; however, rapid degradation during cycling nullifies the

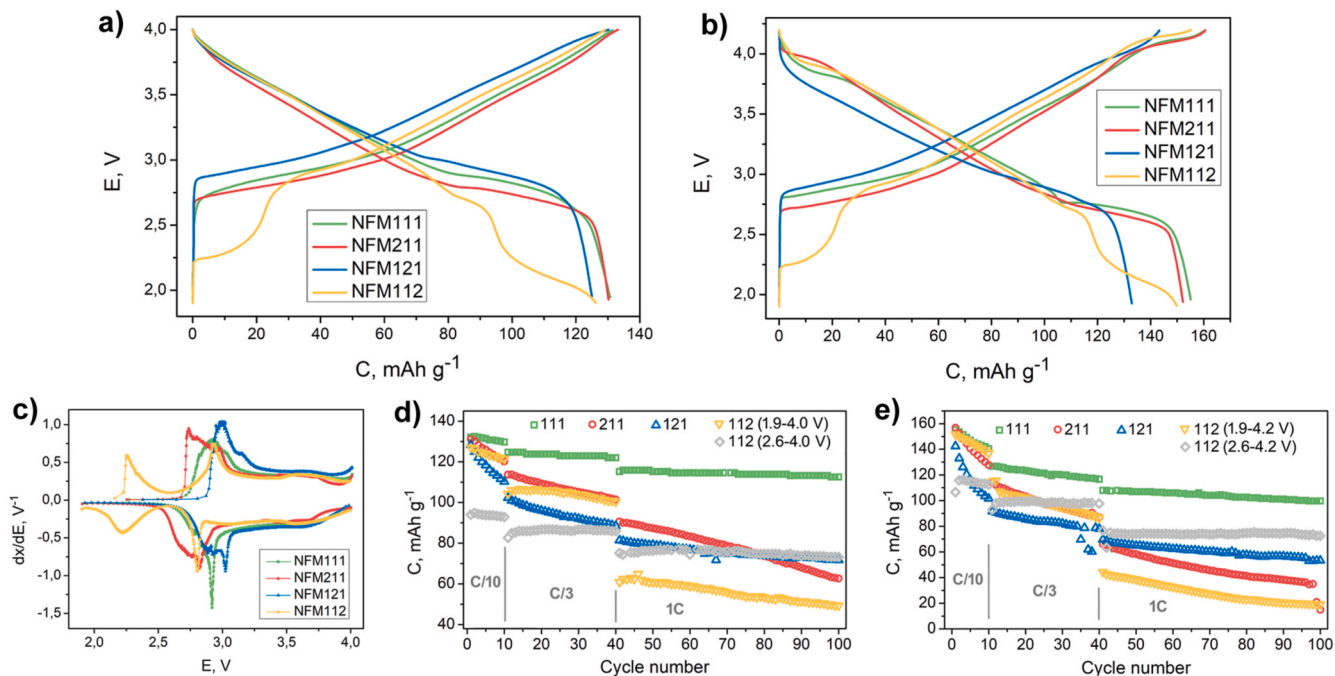


Fig. 2. Charge/discharge curves for the second cycle at C/10 current density in the voltage range of 1.9–4.0 V (a) and 1.9–4.2 V (b); differential capacity curves for the 1.9–4.0 V range (c); capacity retention upon cycling within the 1.9–4.0 V (d) and 1.9–4.2 V (e) voltage ranges. For the NFM112 material, additional data for 2.6–4.0 V and 2.6–4.2 V are also shown.

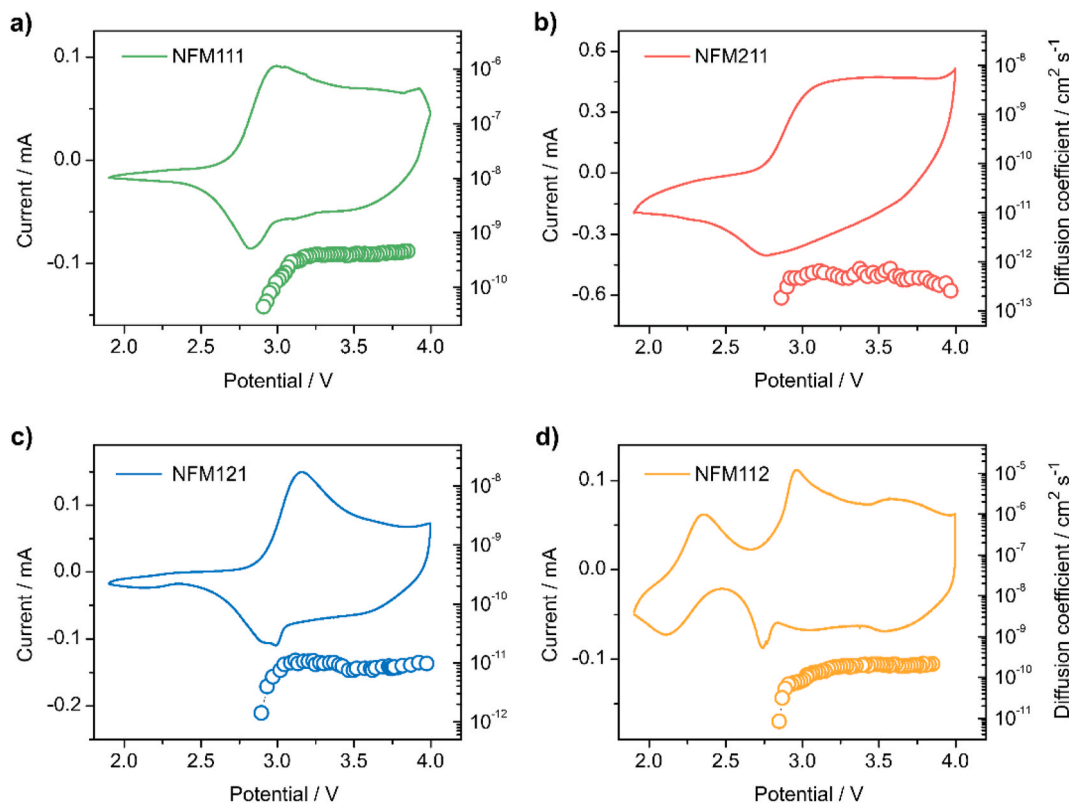


Fig. 3. CVs and diffusion coefficients for (a) NFM111, (b) NFM211, (c) NFM121, and (d) NFM112 electrodes.

advantages of the extended potential range. It was shown that hexagonal-to-monoclinic phase transition associated with migration of d-cations into the Na layer is the most possible reason for such degradation [14–17].

It is known that the capacity degradation of oxide materials during

cycling can be partially suppressed by adding cations that do not exhibit electrochemical activity within the operating potentials but (Ti^{4+} , Nb^{5+} etc.), or by creating a specific morphology of particles [18–22]. Nevertheless, we believe that varying the ratio of Fe, Mn and Ni in a wide range could be crucial for investigating the reasons of deterioration and

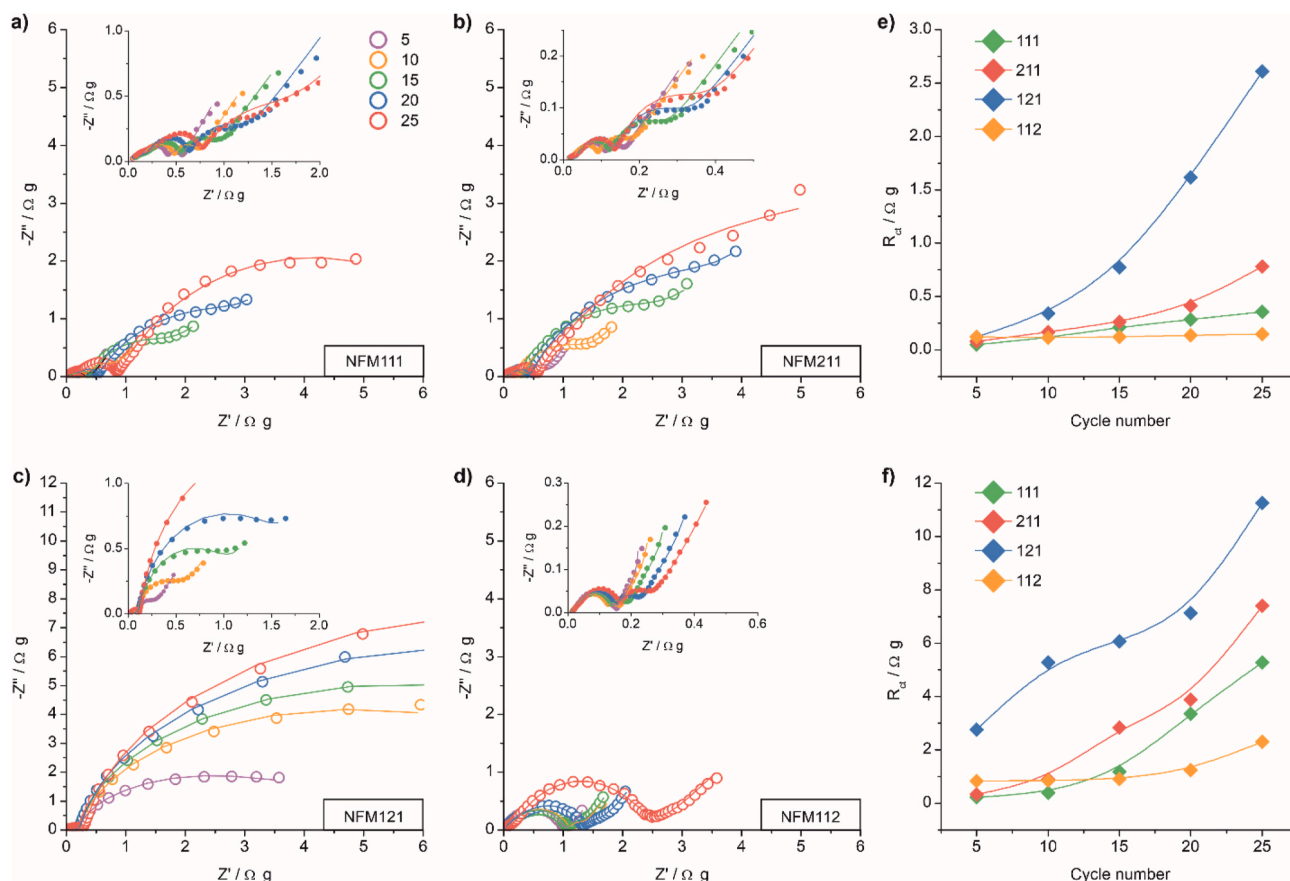


Fig. 4. Electrochemical impedance spectra of (a) NFM111, (b) NFM211, (c) NFM121, and (d) NFM112 electrodes recorded at 3.9 V after 5, 10, 15, 20, and 25 cycles at a rate of C/5 in the 1.9–4.2 V potential range. The insets show the spectra registered under the identical conditions after cycling up to 4.0 V. Plots of the charge transfer resistance (R_{ct}) vs. the cycle number for the studied electrodes during cycling at a rate of C/5 in the potential ranges of 1.9–4.0 V (e) and 1.9–4.2 V (f).

improving electrochemical performance of these materials. In this work, we accurately analyzed the effect of the Mn, Fe, and Ni ratio on the electrochemical properties, thermal stability, and kinetics of Na^+ (de) intercalation in $\text{O3-Na}(\text{Ni,Fe,Mn})\text{O}_2$ oxides.

2. Experimental

2.1. Materials synthesis and characterization

For the synthesis of the $\text{O3-NaNi}_{1-x-y}\text{Fe}_x\text{Mn}_y\text{O}_2$ samples, $\text{NiSO}_4 \cdot 6\text{H}_2\text{O}$ ($\geq 98\%$, Sigma-Aldrich), $\text{MnSO}_4 \cdot \text{H}_2\text{O}$ ($\geq 99\%$, Sigma-Aldrich) and $\text{FeSO}_4 \cdot 7\text{H}_2\text{O}$ ($\geq 99\%$, Sigma-Aldrich) were dissolved in deionized water in an appropriate molar ratio in air at room temperature. Sodium carbonate ($\geq 99.5\%$, Sigma-Aldrich) solution (0.6 M) was immediately added (as a result, the pH value increased from ≈ 4 to ≈ 8) and the obtained $(\text{Ni}_{1-x-y}\text{Fe}_x\text{Mn}_y)\text{CO}_3$ suspension was heated to $160\text{ }^\circ\text{C}$ in a sealed Teflon-lined stainless steel autoclave and conditioned at this temperature for 12 h. The carbonate precipitate was washed, dried, mixed with Na_2CO_3 taken with 5% excess (in the molar ratio of 1:0.525) and annealed at $850\text{ }^\circ\text{C}$ for 10 h in air to obtain $\text{O3-NaNi}_{1-x-y}\text{Fe}_x\text{Mn}_y\text{O}_2$ ($x = y = 0.33$; $x = 0.5$, $y = 0.25$ and $x = 0.25$, $y = 0.5$). To obtain nickel-rich $\text{O3-NaNi}_{1-x-y}\text{Fe}_x\text{Mn}_y\text{O}_2$ ($x = 0.25$, $y = 0.25$), the carbonate precipitate was annealed at $500\text{ }^\circ\text{C}$ under pure O_2 (99.5%), then mixed with NaNO_3 taken with 5% excess (in the molar ratio of 1:1.05) and annealed at $800\text{ }^\circ\text{C}$ for 12 h under pure O_2 (99.5%). All samples were taken out of the furnace without cooling, and immediately transferred into an argon-filled glove box.

The phase composition of the obtained samples was characterized using powder X-ray diffraction in air (PXRD, Huber Guinier camera

G670, $\text{CuK}\alpha_1$ radiation, $\lambda = 1.5406\text{ \AA}$). LeBail fitting and Rietveld refinement were performed using Jana2006 software [23]. The observation of particles size and morphology was carried out using a JEOL JSM-6490LV scanning electron microscope (30 kV, W-cathode).

Samples for transmission electron microscopy (TEM) were prepared by crushing the materials with dimethyl carbonate (DMC) in an agate mortar and then depositing a few drops of the suspension onto copper grids coated with a holey carbon layer. High angle annular dark field scanning transmission electron microscopy (HAADF-STEM) images and energy-dispersive X-ray (EDX) spectra were registered with a Titan Themis Z microscope operated at 200 kV and equipped with a Super-X EDX system.

Using a Netzsch DSC 204 F1 Phoenix instrument, differential scanning calorimetry (DSC) was carried out within a $50\text{--}450\text{ }^\circ\text{C}$ temperature range with a heating rate of $5\text{ }^\circ\text{C min}^{-1}$, in hermetically sealed high-pressure Cr-Ni stainless steel crucibles and in an argon atmosphere. Electrodes from fully charged “half-cells” were extracted, washed with DMC, and dried under vacuum. The dried electrode powders were placed into the crucibles. The crucibles with the samples were hermetically sealed in a dry-argon glove box. To calculate the magnitude of the heat effect, we used the area under the peak on the DSC curve after subtracting the background in Netzsch Proteus software.

2.2. Electrochemical studies

$\text{O3-NaNi}_{1-x-y}\text{Fe}_x\text{Mn}_y\text{O}_2$ -based electrodes were prepared by mixing 76 wt% of the active compound, 12 wt% of carbon black (Timcal Super C 65) and 12 wt% of polyvinylidene fluoride (PVDF, Solvay Solef 5130) binder in N-methylpyrrolidone and spreading it on an aluminum foil by

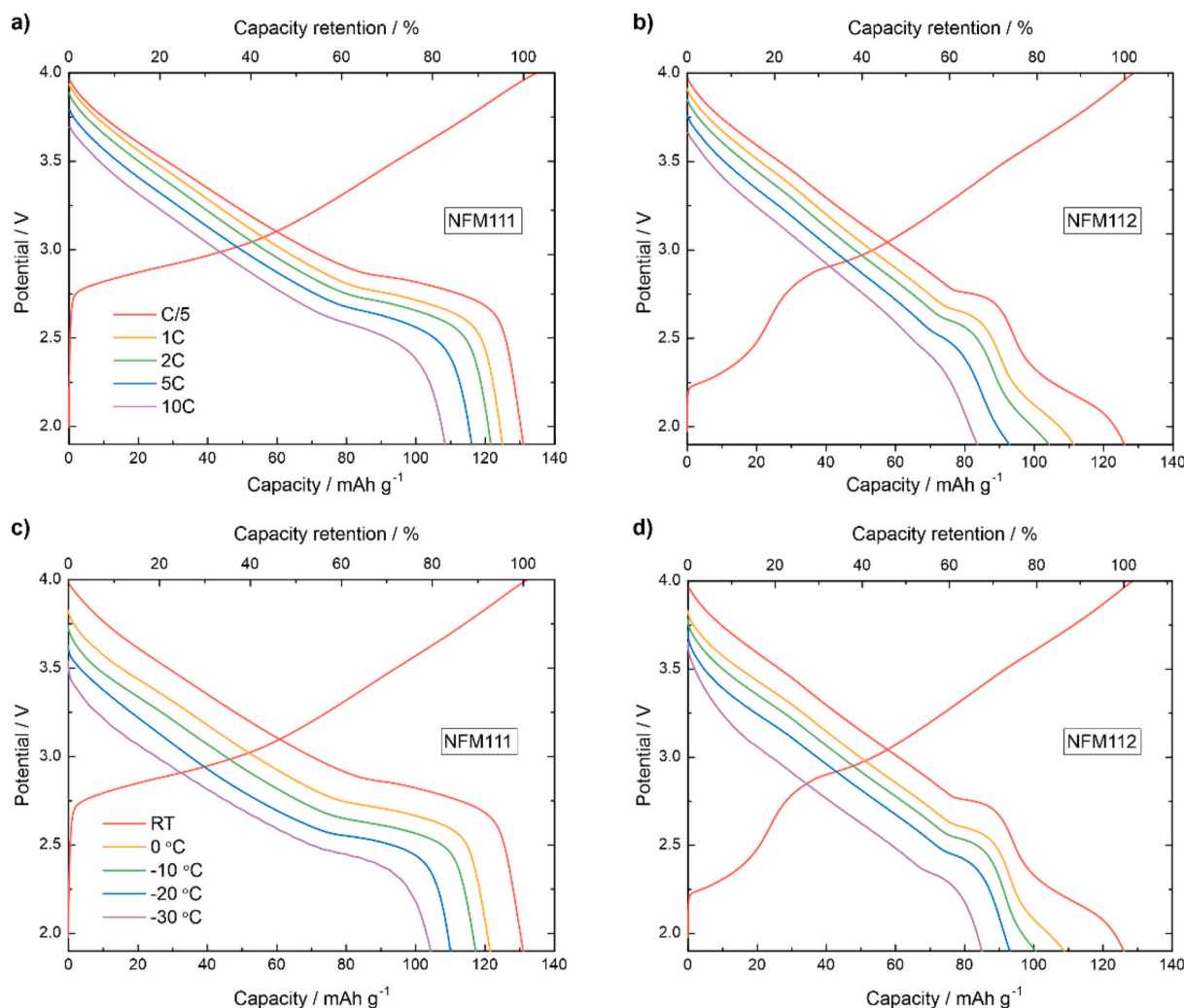


Fig. 5. Charge-discharge curves of NFM111 and NFM112 at different C-rates (charge at C/5 and discharge at C/5, 1C, 2C, 5C, 10C) and low temperatures (charge at RT at C/5 and subsequent discharge at C/5 at 0, -10, -20, -30 °C).

doctor blade technique.

Dried electrodes (mass loading 5–7 mg/cm²) were rolled, punched to round discs and dried at 110 °C for 12 h under dynamic vacuum. Two-electrode stainless steel coin cells (for galvanostatic cycling, impedance, rate capability and low temperature measurements) and three-electrode cells (for diffusion coefficients determination and cyclic voltammetry) were assembled in an argon-filled glove box with Whatman borosilicate glass microfiber filters of GF/A grade used as separators. Sodium metal was used as a counter electrode and Na₃V₂(PO₄)₃, precycled in galvanostatic mode and charged to a 50 % SOC (3.37 V vs. Na/Na⁺), was used as a reference electrode. All the potentials were further recalculated into the Na/Na⁺ scale. Galvanostatic cycling (1.9–4.2 V vs. Na/Na⁺, C/5–2C rates, where 1C - 120 mA/g), were carried out using an Elins P-20X8 potentiostat-galvanostat (ES8 software) or Neware BTS.

Diffusion coefficients were calculated from the potentiostatic intermittent titration technique (PITT) data, which were registered using three-electrode configuration in the single-phase regions of the intercalation isotherms and treated within the Montella's model equations (the case of cylindrical diffusion) [24,25].

Impedance spectra were registered after each 5th galvanostatic cycle in a two-electrode coin cell in the potential ranges of 1.9–4.0 or 1.9–4.2 V after 1 h at the potential of 3.9 V. The measurements were performed with 5 mV alternating voltage amplitude in the frequency range of 10 mHz–100 kHz. The spectra were fitted to a R(RC)(RC)(RC) circuit to account for resistance of electrolyte and electrode, charge transfer at the

anode/electrolyte interphase, transport through the surface layers and charge transfer across the cathode/electrolyte interphase.

PITT and EIS measurements were carried out using a Biologic VMP-3 potentiostat.

The electrolyte used for the charge/discharge, PITT and impedance measurements was 1 M NaPF₆ (Kishida Chemical, battery grade) in propylene carbonate (Sigma Aldrich, anhydrous, ≥ 99.0 %), with 3 % fluoroethylene carbonate (Xiamen TOB New Energy Technology, ≥ 99.95 %). For the low temperature and rate capability measurements, the electrolyte was 1 M NaPF₆ in a 1/1 v/v mixture of ethylene carbonate (Sigma-Aldrich, 99 %, anhydrous) and propylene carbonate with 5 % fluoroethylene carbonate. This composition was used to efficiently passivate the Na anode and minimize the contribution of the polarization component from the counter electrode to the observed behavior under high discharge currents/low temperatures.

For low temperature experiments, cells were precycled at room temperature (RT) (mode: 1 h rest, charge-discharge-charge at C/5). Each pre-cycled cell was discharged at low temperature only once. In high-rate experiments, the cells were charged at C/5 prior to each high-rate discharge. Temperature was controlled with ST 1 B SMART and ZLN-T 125 thermostats (Pol-Eko Aparatura). Reproducibility of results was supported by at least two sets of converging data.

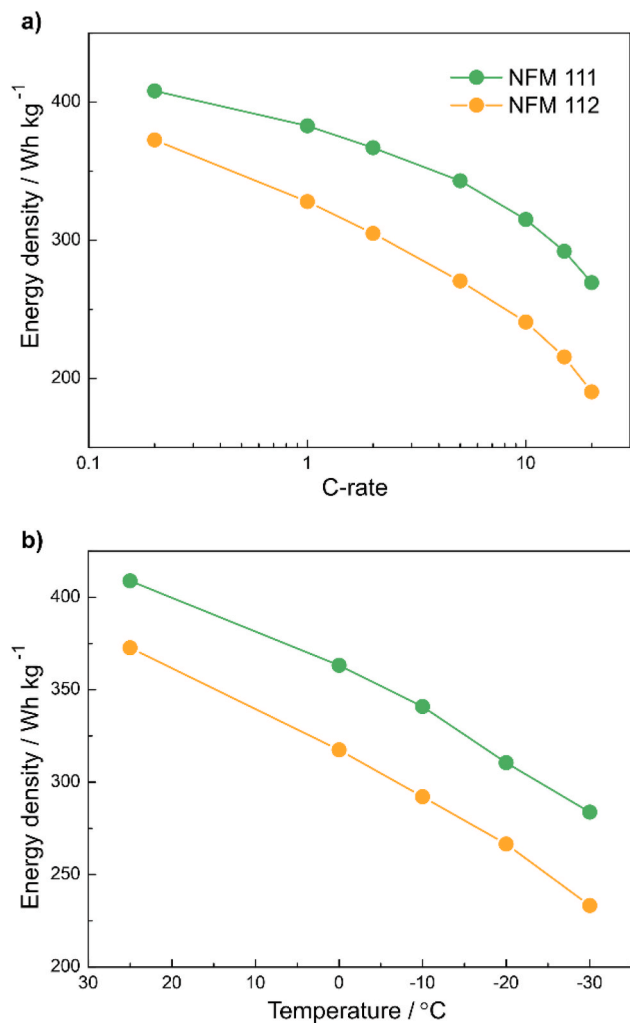


Fig. 6. Energy densities of NFM111 and NFM112 at high discharge currents and at low temperatures.

3. Results and discussion

3.1. Synthesis and basic characterization

The samples with equimolar Ni/Fe/Mn ratio (NFM111), as well as Fe-rich oxide (NFM121), contain single O3-phase after high-temperature annealing. Preparation of NFM211 can only be conducted in oxygen and with using NaNO₃ as an additional oxidizer instead of Na₂CO₃. Attempts to prepare NFM112 with the stoichiometric Na:(Ni, Fe, Mn) = 1:1 ratio by annealing in air or Ar failed, but reducing the Na content to the Na_{0.75}Ni_{0.25}Fe_{0.25}Mn_{0.5}O₂ composition provided a single-phase sample through air annealing. However, slight broadening of the reflections in the PXRD pattern may indicate formation of the P3-phase domains, since the sodium content in as-prepared NFM112 is intermediate between the typical values for the O3 and P3 phases [9].

PXRD patterns of the obtained samples are shown in Fig. 1. Unit cell parameters determined by means of Le Bail and Rietveld refinement are given in Table 1.

The morphology of all the samples is quite similar: they consist of micron-sized plate-like particles (Fig. 1 b-e). The uniform distribution of d-metals in NFM111, NFM121 and NFM112 was confirmed in the STEM-EDX experiments (Fig. 1 f-i). The nickel-enriched NFM211 sample exhibits gradient morphology with increasing nickel concentration at the surface of the particles (Fig. 1g). The ratio of d-elements determined using STEM-EDX correlates very well with the composition loaded

during the synthesis of the samples (Table S1).

All samples except NFM211 crystallize in trigonal crystal system with *R-3m* space group. Sample NFM112 with the sodium content close to stoichiometric one (≈ 0.95 Na per f.u.) was obtained by discharge in an electrochemical sodium half-cell to a potential of 1.9 V; its unit cell parameters are also given in Table 1. Nickel-rich NFM211 sample has the same structure as NaNiO₂ and its PXRD pattern can be refined using monoclinic *C2/m* space group. Examples of monoclinic splitting of the PXRD reflections are given in Fig. S4. Similar results were obtained by Wang et al.: PXRD patterns for NaFe_{1-x}Ni_xO₂ for $x = 0, 0.5, 0.6,$ and 0.7 were indexed in trigonal *R-3m* space group, and for $x = 0.8$ and 0.9 – in monoclinic *C2/m* [26]. Detailed information on Le Bail and Rietveld refinement of the PXRD patterns is given in Supplementary Materials (Figs. S1–S6, Tables S2–S5).

All studied materials demonstrate reversible capacity of 125–131 mAh·g⁻¹ within 1.9–4.0 V voltage range (Fig. 2a). Increasing upper voltage limit up to 4.2 V results in the growth of initial capacity up to 145, 150, 156 and 157 mAh·g⁻¹ for NFM121, NFM112, NFM211 and NFM111, respectively (Fig. 2b). Corresponding Coulombic efficiency values are presented in Fig. S7.

An analysis of the differential capacity curves (Fig. 2c) leads to the following features of the studied systems: i) the NFM211 sample which was obtained under the most oxidizing conditions and should contain Ni³⁺ in the discharged state has the lowest average working potential; ii) the NFM121 sample which should contain cations in the same oxidation states as NFM111 begins to oxidize at much higher potential (≈ 0.2 V difference) than the latter. The observed effects can be explained by taking into account previously described phenomena concerning mutual influence of Ni and Fe cations, and hybridization of oxygen 2p valence band and e_g band of Ni³⁺ cation in oxides [15,17,26–30]. Thus, Nunba et al. observed so-called “redox paradox” in nickel-containing NaTi_{0.45}Ni_{0.55}O₂ and NaFe_{0.5}Ni_{0.5}O₂ oxides, due to which the oxidation of Ni³⁺ occurs at lower potentials than Ni²⁺ [27]. Effects observed in our work can be explored in more detail in subsequent studies using such methods as Mössbauer spectroscopy, X-ray absorption spectroscopy and DFT calculations.

Cycling stability of the studied materials depends strongly on the ratio of d-cations in the structure and on the voltage range. For the 1.9–4.0 V range, stoichiometric NFM111 composition demonstrates the lowest capacity loss: 2.0, 2.1 and 2.8 % after 10 cycles at C/10 rate, 30 cycles at C/3 and 60 cycles at 1C, respectively (0.2, 0.07 and 0.05 % per cycle), see Fig. 2d. Fe-rich and Ni-rich samples degrade with much higher rates, but the NFM112 material exhibits ambiguous behavior. We found a fairly strong decrease in capacity with increasing current density from C/10 to C/3 and further to 1C, and assumed that it can be due to degradation associated with the process occurring at 2.0–2.5 V. Limiting the lower potential limit to 2.6 V, we obtained excellent cyclability of the material and quite low drop in capacity with increasing current. However, initial capacity of NFM112 is reduced to ≈ 95 mAh·g⁻¹ in this case.

It is known that an increase in the upper potential limit upon galvanostatic cycling of the layered cathode materials leads to an additional plateau at ~ 4.0 V, which increases the capacity by ~ 30 mAh·g⁻¹ (Fig. 2b), but also leads to accelerated degradation (Fig. 2e) [15–17]. However, the sample of stoichiometric composition NFM111 again demonstrates the best stability, while nickel- and iron-enriched oxides quickly degrade. In the case of manganese-rich NFM112 material, Mn³⁺/Mn⁴⁺ redox also leads to pure capacity retention. When lower potential limit is fixed at 1.9 V, the cell lose 11, 26 and 60% of its capacity after 10 cycles at current density C/10, 30 cycles at C/3 and 60 at 1C, respectively. At the same time, when the lower limit of the potential is raised to 2.6 V, the drop in capacity associated with an increase in current density is significantly reduced, and degradation practically disappears, especially at current densities of C/3 and 1C.

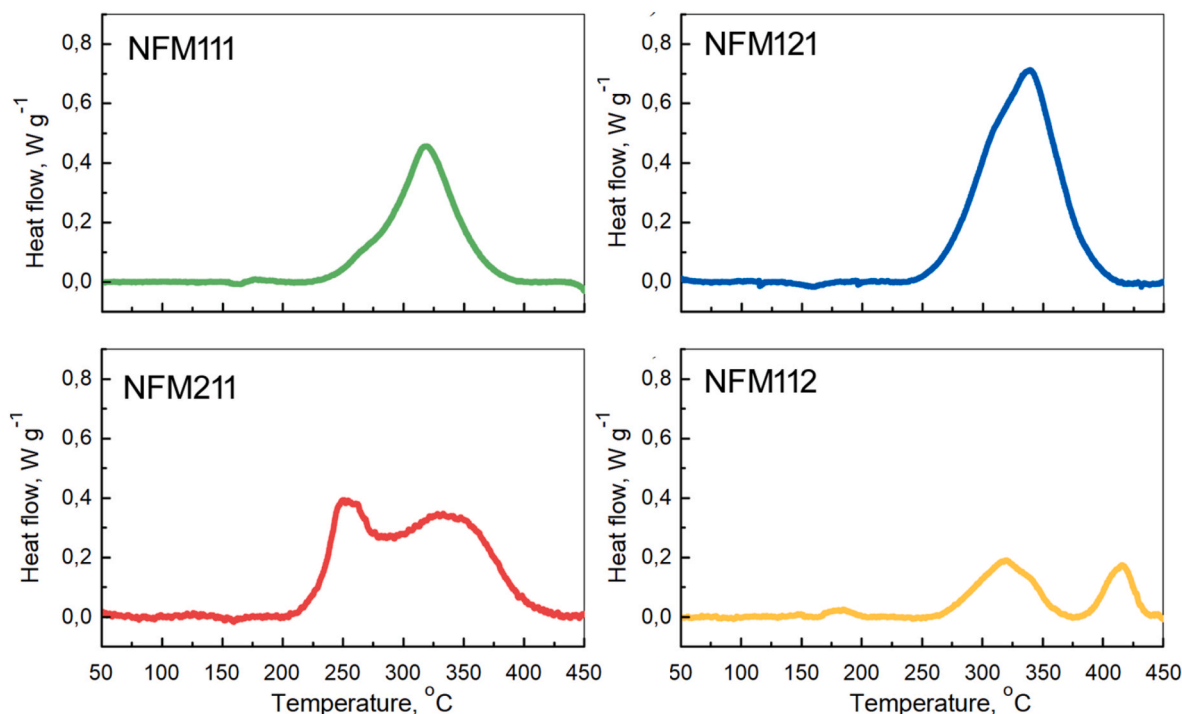


Fig. 7. Results of the DSC experiment within 50–450 °C temperature interval for the electrodes charged to 4.0 V vs. Na/Na⁺. Remaining sodium content is 0.45–0.48 Na⁺ per f.u. DSC curves are given after subtracting the background line.

Table 2

DSC data for the electrodes charged to 4.0 V.

Composition	Peak onset temperature, °C	Peak temperature, °C	Enthalpy 50–450 °C, J g ⁻¹
NFM111	233	267, 319	319
NFM211	207	254, 353	584
NFM121	247	308, 340	620
NFM112	266	323, 417	179

3.2. Detailed electrochemical study

A more detailed electrochemical study was performed to evaluate the influence of the chemical composition on the kinetics of sodium (de)intercalation, and on resistivity of the interfaces and cycling stability.

Fig. 3 shows cyclic voltammograms (CVs) of the studied electrodes. For all the materials, a pair of peaks is observed at 2.9–3.0 V, corresponding to phase transitions [15,31,32]. For the Mn-enriched sample (NFM112), a pair of peaks is also observed at about 2.25 V, which also corresponds to a phase transformation. To characterize the transport properties of the layered oxides, the diffusion coefficients of sodium ions were measured by PITT using the procedure, which allows to account for finite rates of charge transfer and uncompensated ohmic drop [24,25]. The diffusion length parameter (0.5 μm; assumed equal for all samples) was estimated from the SEM and TEM data. Diffusion coefficients were calculated in the single-phase regions of the isotherms while scanning the potential from 4.0 V to the potential of the phase transformation (~2.9–3.0 V), which is associated with a steep diminution of the diffusion coefficient value (Fig. 3). For NFM111 (Fig. 3a) and NFM112 (Fig. 3d), apparent diffusion coefficients are close and fall in the range of 1·10⁻¹⁰–5·10⁻¹⁰ cm² s⁻¹. For the NFM121 composition (Fig. 3c), the effective diffusion coefficients are much lower: 3·10⁻¹²–1·10⁻¹¹ cm² s⁻¹. The lowest Na-ion diffusivities of 3·10⁻¹³–5·10⁻¹³ cm² s⁻¹ are found for the NFM211 material (Fig. 3b). Slow kinetics of sodium deintercalation in the nickel-enriched sample can be associated both with certain morphological inhomogeneities and with already

mentioned participation of oxygen anions in the redox process [27].

As it was mentioned above, to assess the stability of the electrochemical characteristics of the materials, two potential ranges of 1.9–4.0 V and 1.9–4.2 V vs. Na/Na⁺ were chosen. High-voltage plateau is associated with a phase transition, which translates into a pair of peaks with high peak-to-peak separations in the CVs registered in three-electrode cells with a wider anodic cutoff limit (Fig. S8). Correspondingly, a pair of peaks is observed for all electrodes at a formal potential of about 4.0 V, corresponding to the P3/OP2 phase transition [15,31,32].

The changes in kinetic parameters during electrode cycling in the potential intervals with anodic limits of 4.0 and 4.2 V were evaluated using electrochemical impedance spectroscopy. The electrochemical impedance spectra of the NFM electrodes were recorded at 3.9 V after every 5 cycles in two-electrode cells. The Nyquist plots for all studied samples after a different number of cycles up to 4.2 V are shown in Fig. 4a–d (insets show the spectra measured after cycling with 4.0 V anodic limit).

The spectra registered in two-electrode cells show skewed semicircles at high frequencies, which reflect the contributions from the charge transfer at the Na anode/electrolyte interface and ion transport through the solid electrolyte interface and cathode/electrolyte interface [33]. This high frequency region undergoes minor changes after continuous cycling for all the materials in both potential windows (Fig. 4a–d). The most prominent changes occur in the region of medium and low frequencies, where the diameter of the observed semicircle shows large variation during cycling. Based on the observed dependence of the diameter of this semicircle on the potential, it can be attributed to the interfacial charge transfer resistance (R_{ct}). Fig. 4e and f shows the changes in R_{ct} during cycling in the potential ranges of 1.9–4.0 V and 1.9–4.2 V.

After undergoing 25 cycles at C/5 within the potential range of 1.9–4.0 V, the NFM111 and NFM211 materials experience a 7 and 10-fold increase in R_{ct} value, respectively (Fig. 4e). The Fe-enriched sample displays maximal changes, with an increase of approximately 20 times. Interestingly, the Mn-enriched material only experiences a 15 %

rise in R_{ct} , indicating a low reactivity of the NFM112 surface towards the formation of resistive interfaces upon the surface restructuring. In the case of anodic limit of 4.2 V, the largest values of R_{ct} (11.3 Ohm·g) are again observed for the NFM121 material. A 20-fold increase in R_{ct} is also characteristic of NFM211 and NFM111, while the NFM112 material shows a very moderate twofold increase in R_{ct} after 25 cycles, which supports a conjecture on minimal surface restructuring with an increase in the anodic potential limit, accompanied by an increase in the barrier of interfacial ion transfer. The weak increase in charge transfer resistance at the electrode-electrolyte interface suggests that the degradation of the NFM112 material observed during long-term cycling (Fig. 2d and e) is associated primarily with the transformation of its crystal structure (e.g., formation of defects) leading to increase in internal diffusion limitations that accumulate in the material during cycling. Taking into account the suppression of degradation that we observed when the lower potential limit was increased from 1.9 to 2.6 V, we can conclude that these structural changes can appear due to the Mn^{3+}/Mn^{4+} redox associated with significant volume change. Previously, similar behavior was observed for lithium-containing spinels during lithiation of $LiNi_{0.5}Mn_{1.5}O_4$ [34–36].

3.3. Low temperature and high-rate performance

After identifying NFM111 and NFM112 as the most promising compositions in terms of ionic diffusivities and interfacial resistances during continuous cycling, we investigated their electrochemical behavior at high discharge currents and low temperatures within the potential range of 1.9–4.0 V. Both materials exhibited impressive rate capability, as shown in Fig. 5a and b. NFM111 retains ca. 83 % (108 mAh·g⁻¹) of its initial capacity at 10C, while the high-rate performance of NFM112 is slightly worse amounting to 66 % (83 mAh·g⁻¹) at 10C.

Similar trends are observed at low temperatures (Fig. 5c and d). At –30 °C, NFM111 and NFM112 retain ca. 80 % (104 mAh·g⁻¹) and 67 % (85 mAh·g⁻¹) of their capacity at r.t., respectively. This demonstrates the potential for these materials to be used in challenging low temperature conditions. Fig. 6 illustrates the energy density plots of NFM111 and NFM112 vs. C-rate and temperature. NFM111 offers a 10 % increase in energy density compared to NFM112, which remains almost constant at C-rates up to 20 C and at temperatures as low as –30 °C as the plots for the energy density vs. the respective parameter are almost parallel.

3.4. Thermal stability study

Varying the ratio of 3d-metals in $NaNi_xFe_yMn_{1-x-y}O_2$ layered oxides not only leads to a change in their electrochemical properties, but also affects the thermal stability. The thermal stability of the materials in charged state is extremely important issue, especially when it comes to sodium-ion batteries for large-scale energy storage [37,38]. In this regard, we studied the dependence of the decomposition temperature and enthalpy on the composition for the electrodes charged to 4.0 V. The results of DSC experiments are shown in Fig. 7.

All samples show at least two decomposition peaks with the position varying over a wide temperature range. The peak with the lowest temperature (≈ 250 °C) was observed for the nickel-enriched NFM211 oxide, and with the highest temperature (≈ 415 °C) - for the manganese-enriched one. This suggests that the decomposition process is multi-stage, and the oxide with high nickel content begins to decompose first. Increasing the iron content also leads to a decrease in stability compared to NFM111. In contrary, the charged NFM112 material starts to decompose at higher temperature with two peaks at 322 °C and 417 °C, and the released enthalpy is only 179 J g⁻¹, which is significantly lower than that for other materials (see Table 2). The main reason for such behavior is high stability of Mn^{4+} in oxides: for the charged lithium-based NMC111 cathode material, Nam et al. demonstrated that manganese retains +4 oxidation state up to 400 °C, while nickel is reduced from +4 to +2 after reaching 200 °C [39]. In addition, an increase in

nickel amount in NMC relative to cobalt and manganese decreases the oxygen evolution temperature and increases its amount [40–42].

It is worth noting that Fe^{4+} is also unstable as it easily oxidizes oxygen anions due to strong hybridization of Fe 3d and O 2p orbitals. Oxygen evolution was found for both $LiFeO_2$ and $NaFeO_2$ during deintercalation of alkali ions; therefore, low thermal stability of the NFM121 sample is not surprising [10,43,44].

4. Conclusions

Layered O3-type oxide cathode materials $NaNi_{1/3}Fe_{1/3}Mn_{1/3}O_2$ (NFM111), $NaNi_{0.5}Fe_{0.25}Mn_{0.25}O_2$ (NFM211), $NaNi_{0.25}Fe_{0.5}Mn_{0.25}O_2$ (NFM121) and $NaNi_{0.25}Fe_{0.25}Mn_{0.5}O_2$ (NFM112) were studied for their phase composition, electrochemical properties and thermal stability. Our study demonstrates that only Mn has a clear positive effect on such important electrochemical properties as cyclic stability and thermal safety. Increase in Ni amount reduces average working potential and the kinetics of sodium (de)intercalation, and lowers the onset temperature of thermal decomposition, which makes nickel-rich oxides potentially dangerous for large size power sources. Excess of iron also reduces the cyclic stability and leads to large heat release from the charged electrode. Thus, we conclude that the optimal ratio of all these cations is close to equimolar or with slight excess of manganese. Such materials are safer, more stable during cycling, tolerant to low-temperature and high-rate discharge and should become the basis for the subsequent development of sodium-ion batteries.

CRedit authorship contribution statement

Vitalii A. Shevchenko: Conceptualization, Formal analysis, Investigation, Visualization, Writing – original draft. **Alena I. Komayko:** Investigation, Writing – review & editing. **Elizaveta V. Sivenkova:** Investigation, Writing – review & editing. **Ruslan R. Samigullin:** Investigation, Writing – review & editing. **Irina A. Skvortsova:** Investigation, Writing – review & editing. **Artem M. Abakumov:** Conceptualization, Methodology, Writing – review & editing. **Viktoriya A. Nikitina:** Conceptualization, Methodology, Writing – review & editing. **Oleg A. Drozhzhin:** Conceptualization, Investigation, Methodology, Visualization, Writing – original draft, Writing – review & editing. **Evgeny V. Antipov:** Funding acquisition, Project administration, Writing – review & editing.

Declaration of competing interest

The authors declare that they have no known competing financial interests or personal relationships that could have appeared to influence the work reported in this paper.

Data availability

Data will be made available on request.

Acknowledgments

This work was supported by the Russian Science Foundation (grant no. 17-73-30006) and M.V. Lomonosov Moscow State University Program of Development.

Appendix A. Supplementary data

Supplementary data to this article can be found online at <https://doi.org/10.1016/j.jpowsour.2024.234092>.

References

- [1] J.-Y. Hwang, S.-T. Myung, Y.-K. Sun, Sodium-ion batteries: present and future, *Chem. Soc. Rev.* 46 (2017) 3529–3614, <https://doi.org/10.1039/c6cs00776g>.
- [2] I. Hasa, S. Mariyappan, D. Saurel, P. Adelhelm, A.Y. Kuposov, C. Masquelier, L. Croguennec, M. Casas-Cabanas, Challenges of today for Na-based batteries of the future: from materials to cell metrics, *J. Power Sources* 482 (2021) 228872, <https://doi.org/10.1016/j.jpowsour.2020.228872>.
- [3] A. Rudola, A.J.R. Rennie, R. Heap, S.S. Meysami, A. Lowbridge, F. Mazzali, R. Sayers, C.J. Wright, J. Barker, Commercialisation of high energy density sodium-ion batteries: faradion's journey and outlook, *J. Mater. Chem.* 9 (2021) 8279–8302, <https://doi.org/10.1039/d1ta00376c>.
- [4] E.J. Kim, P.R. Kumar, Z.T. Gossage, K. Kubota, T. Hosaka, R. Tatara, S. Komaba, Active material and interphase structures governing performance in sodium and potassium ion batteries, *Chem. Sci.* 13 (2022) 6121–6158, <https://doi.org/10.1039/D2SC00946C>.
- [5] K. Mizushima, P.C. Jones, P.J. Wiseman, J.B. Goodenough, Li_xCoO_2 ($0 < x < 1$): a new cathode material for batteries of high energy density, *Mater. Res. Bull.* 15 (1980) 783–789, [https://doi.org/10.1016/0025-5408\(80\)90012-4](https://doi.org/10.1016/0025-5408(80)90012-4).
- [6] Delmas, D. Carlier, M. Guignard, The layered oxides in lithium and sodium-ion batteries: a solid-state chemistry approach, *Adv. Energy Mater.* 11 (2021) 2001201–2001220, <https://doi.org/10.1002/aenm.202001201>.
- [7] J. Liu, J. Wang, Y. Ni, K. Zhang, F. Cheng, J. Chen, Recent breakthroughs and perspectives of high-energy layered oxide cathode materials for lithium ion batteries, *Mater. Today* 43 (2021) 132–165, <https://doi.org/10.1016/j.mattod.2020.10.028>.
- [8] L. Croguennec, M.R. Palacin, Recent achievements on inorganic electrode materials for lithium-ion batteries, *J. Am. Chem. Soc.* 137 (9) (2015) 3140–3156, <https://doi.org/10.1021/ja507828x>.
- [9] K. Kubota, S. Kumakura, Y. Yoda, K. Kuroki, S. Komaba, Electrochemistry and solid-state chemistry of NaMeO_2 ($\text{me} = 3\text{d transition metals}$), *Adv. Energy Mater.* 8 (2018) 1703415, <https://doi.org/10.1002/aenm.201703415>.
- [10] X. Gao, H. Liu, W. Deng, Y. Tian, G. Zou, H. Hou, X. Ji, Iron-based layered cathodes for sodium-ion batteries, *Batteries & Supercaps* 4 (2021) 1657–1679, <https://doi.org/10.1002/batt.202100108>.
- [11] N. Yabuuchi, M. Yano, H. Yoshida, S. Kuze, S. Komaba, Synthesis and electrode performance of O3-type NaFeO_2 - $\text{NaNi}_{1/2}\text{Mn}_{1/2}\text{O}_2$ solid solution for rechargeable sodium batteries, *J. Electrochem. Soc.* 160 (2013) A3131–A3137, <https://doi.org/10.1149/2.018305jes>.
- [12] J.Y. Hwang, S.T. Myung, D. Aurbach, Y.K. Sun, Effect of nickel and iron on structural and electrochemical properties of O3 type layer cathode materials for sodium-ion batteries, *J. Power Sources* 324 (2016) 106–112, <https://doi.org/10.1016/j.jpowsour.2016.05.064>.
- [13] C. Zhao, F. Ding, Y. Lu, L. Chen, Y.-S. Hu, High-entropy layered oxide cathodes for sodium-ion batteries, *Angew. Chem. Int. Ed.* 59 (2020) 264–269, <https://doi.org/10.1002/anie.201912171>.
- [14] Y. Xie, H. Wang, G. Xu, J. Wang, H. Sheng, Z. Chen, Y. Ren, Cheng-Jun Sun, J. Wen, J. Wang, D.J. Miller, J. Lu, K. Amine, Zi-Feng Ma, Operando XRD and TXM study on the metastable structure change of $\text{NaNi}_{1/3}\text{Fe}_{1/3}\text{Mn}_{1/3}\text{O}_2$ under electrochemical sodium-ion intercalation, *Adv. Energy Mater.* 6 (2016) 1601306, <https://doi.org/10.1002/aenm.201601306>.
- [15] M. Jeong, H. Lee, J. Yoon, W.S. Yoon, O3-type $\text{NaNi}_{1/3}\text{Fe}_{1/3}\text{Mn}_{1/3}\text{O}_2$ layered cathode for Na-ion batteries: structural evolution and redox mechanism upon Na (de) intercalation, *J. Power Sources* 439 (2019) 227064, <https://doi.org/10.1016/j.jpowsour.2019.227064>.
- [16] X. Li, Y. Wang, D. Wu, L. Liu, S.-H. Bo, G. Ceder, Jahn–teller assisted Na diffusion for high performance Na ion batteries, *Chem. Mater.* 28 (18) (2016) 6575–6583, <https://doi.org/10.1021/acs.chemmater.6b02440>.
- [17] V.A. Shevchenko, I.S. Glazkova, D.A. Novichkov, I. Skvortsova, A.V. Sobolev, A. M. Abakumov, I.A. Presniakov, O.A. Drozhzhin, E.V. Antipov, Competition between the Ni and Fe redox in the O3- $\text{NaNi}_{1/3}\text{Fe}_{1/3}\text{Mn}_{1/3}\text{O}_2$ cathode material for Na-ion batteries, *Chem. Mater.* 35 (10) (2023) 4015–4025, <https://doi.org/10.1021/acs.chemmater.3c00338>.
- [18] L. Tan, Q. Wu, Z. Liu, Q. Chen, H. Yi, Z. Zhao, L. Song, S. Zhong, X. Wu, L. Li, Ti-substituted O3-type layered oxide cathode material with high-voltage stability for sodium-ion batteries, *J. Colloid Interface Sci.* 622 (2022) 1037–1044, <https://doi.org/10.1016/j.jcis.2022.04.112>.
- [19] R. Yue, F. Xia, R. Qi, D. Tie, S. Shi, Z. Li, Y. Zhao, J. Zhang, Trace Nb-doped $\text{Na}_{0.7}\text{Ni}_{0.3}\text{Co}_{0.1}\text{Mn}_{0.6}\text{O}_2$ with suppressed voltage decay and enhanced low temperature performance, *Chin. Chem. Lett.* 32 (2021) 849–853, <https://doi.org/10.1016/j.ccl.2020.05.025>.
- [20] Y.J. Park, J.U. Choi, J.H. Jo, C.-H. Jo, J. Kim, S.-T. Myung, A new strategy to build a high-performance P2-Type cathode material through titanium doping for sodium-ion batteries, *Adv. Funct. Mater.* 29 (2019) 1901912, <https://doi.org/10.1002/adfm.201901912>.
- [21] K. Zou, M. Jiang, Z. Zhao, S. Xie, T. Ning, L. Tan, H. Li, Y. Zhou, W. Wang, X. Wu, L. Li, Mechanistic insights into suppressing microcracks by regulating grain size of precursor for high-performance Ni-rich cathodes, *Chem. Eng. J.* 476 (2023) 146793, <https://doi.org/10.1016/j.cej.2023.146793>.
- [22] K.R. Chemelewski, E.-S. Lee, W. Li, A. Manthiram, Factors influencing the electrochemical properties of high-voltage spinel cathodes: relative impact of morphology and cation ordering, *Chem. Mater.* 25 (14) (2013) 2890–2897, <https://doi.org/10.1021/cm401496k>.
- [23] V. Petříček, M. Dušek, L. Palatinus, Crystallographic computing system JANA2006: general features, *Zeitschrift für Kristallologie* 229 (2014) 345–352, <https://doi.org/10.1515/zkri-2014-1737>.
- [24] C. Montella, Discussion of the potential step method for the determination of the diffusion coefficients of guest species in host materials, *J. Electroanal. Chem.* 518 (2) (2002) 61–83, [https://doi.org/10.1016/S0022-0728\(01\)00691-X](https://doi.org/10.1016/S0022-0728(01)00691-X).
- [25] C. Montella, Apparent diffusion coefficient of intercalated species measured with PITT, *Electrochim. Acta* 51 (15) (2006) 3102–3111, <https://doi.org/10.1016/j.electacta.2005.08.046>.
- [26] X. Wang, G. Liu, T. Iwao, M. Okubo, A. Yamada, Role of ligand-to-metal charge transfer in O3-type NaFeO_2 - NaNiO_2 solid solution for enhanced electrochemical properties, *J. Phys. Chem. C* 118 (6) (2014) 2970–2976, <https://doi.org/10.1021/jp411382r>.
- [27] Y. Namba, T. Iwao, B. Mortemard de Boisse, W. Zhao, E. Hosono, D. Asakura, H. Niwa, Hi Kiuchi, J. Miyawaki, Y. Harada, M. Okubo, A. Yamada, Redox potential paradox in Na_xMO_2 for sodium-ion battery cathodes, *Chem. Mater.* 28 (4) (2016) 1058–1065, <https://doi.org/10.1021/acs.chemmater.5b04289>.
- [28] A.A. Savina, A.O. Boev, E.D. Orlova, A.V. Morozov, A.M. Abakumov, Nickel is a key element in the future energy, *Russ. Chem. Rev.* (2023) 92, <https://doi.org/10.59761/RCSR5086>.
- [29] N. Li, D.K. Bediako, R.G. Hadt, D. Hayes, T.J. Kempa, F. von Cube, D.C. Bell, L. X. Chen, D.G. Nocera, Influence of iron doping on tetraivalent nickel content in catalytic oxygen evolving films, *Proc. Natl. Acad. Sci. USA* 114 (2017) 1486–1491, <https://doi.org/10.1073/pnas.1620787114>.
- [30] V. Bisogni, S. Catalano, R.J. Green, M. Gilbert, R. Scherwitzl, Y. Huang, V. N. Strocov, P. Zubko, S. Balandeh, J.M. Triscone, G. Sawatzky, T. Schmitt, Ground-state oxygen holes and the metal–insulator transition in the negative charge-transfer rare-earth nickelates, *Nat. Commun.* 7 (2016) 1, <https://doi.org/10.1038/ncomms13017>.
- [31] Y. Xie, H. Gao, R. Harder, L. Li, J. Gim, H. Che, H. Wang, Y. Ren, X. Zhang, L. Li, Z. Chen, K. Amine, Z.-F. Ma, Revealing the structural evolution and phase transformation of O3-type $\text{NaNi}_{1/3}\text{Fe}_{1/3}\text{Mn}_{1/3}\text{O}_2$ cathode material on sintering and cycling processes, *ACS Appl. Energy Mater.* 3 (2020) 6107–6114, <https://doi.org/10.1021/acsaem.0c00475>.
- [32] D.D. Yuan, Y.X. Wang, Y.L. Cao, X.P. Ai, H.X. Yang, Improved electrochemical performance of Fe-substituted $\text{NaNi}_{0.5}\text{Mn}_{0.5}\text{O}_2$ cathode materials for sodium-ion batteries, *ACS Appl. Mater. Interfaces* 7 (2015) 8585–8591, <https://doi.org/10.1021/acsami.5b00594>.
- [33] V.A. Nikitina, Charge transfer processes in the course of metal-ion electrochemical intercalation, *Curr. Opin. Electrochem.* 19 (February 2020) 71–77, <https://doi.org/10.1016/j.coelec.2019.10.006>.
- [34] M. Mancini, G. Gabrielli, P. Axmann, M. Wohlfahrt-Mehrens, Electrochemical performance and phase transitions between 1.5 and 4.9 V of highly-ordered $\text{LiNi}_{0.5}\text{Mn}_{1.5}\text{O}_4$ with tailored morphology: influence of the lithiation method, *J. Electrochem. Soc.* 164 (1) (2017) A6229–A6235, <https://doi.org/10.1149/2.0291701jes>.
- [35] A. Howeling, A. Stoll, D.O. Schmidt, H. Geßwein, U. Simon, J.R. Binder, Influence of synthesis, dopants and cycling conditions on the cycling stability of doped $\text{LiNi}_{0.5}\text{Mn}_{1.5}\text{O}_4$ spinels, *J. Electrochem. Soc.* 164 (1) (2017) A6349–A6358, <https://doi.org/10.1149/2.0521701jes>.
- [36] O.A. Drozhzhin, A.M. Alekseeva, V.A. Shevchenko, D. Chernyshov, A. M. Abakumov, E.V. Antipov, Phase transitions in the “spinel-layered” $\text{Li}_{1+x}\text{Ni}_{0.5}\text{Mn}_{1.5}\text{O}_4$ ($x = 0, 0.5, 1$) cathodes upon (De)lithiation studied with operando synchrotron X-ray powder diffraction, *Nanomaterials* 11 (2021) 1368, <https://doi.org/10.3390/nano11061368>.
- [37] R.R. Samigullin, O.A. Drozhzhin, E.V. Antipov, Comparative study of the thermal stability of electrode materials for Li-ion and Na-ion batteries, *ACS Appl. Energy Mater.* 5 (2022) 14–19, <https://doi.org/10.1021/acsaem.1c03151>.
- [38] D. Velumani, A. Bansal, Thermal behavior of lithium- and sodium-ion batteries: a review on heat generation, battery degradation, thermal runaway – perspective and future directions, *Energy Fuels* 36 (23) (2022) 14000–14029, <https://doi.org/10.1021/acs.energyfuels.2c02889>.
- [39] K.-W. Nam, S.-M. Bak, E. Hu, X. Yu, Y. Zhou, X. Wang, L. Wu, Y. Zhu, K.-Y. Chung, X.-Q. Yang, Combining in situ synchrotron X-ray diffraction and absorption techniques with transmission electron microscopy to study the origin of thermal instability in overcharged cathode materials for lithium-ion batteries, *Adv. Funct. Mater.* 23 (2013) 1047–1063, <https://doi.org/10.1002/adfm.201200693>.
- [40] H. Bang, D.-H. Kim, Y.C. Bae, J. Prakash, Y.-K. Sun, Effects of metal ions on the structural and thermal stabilities of $\text{Li}[\text{Ni}_{1-x-y}\text{Co}_x\text{Mn}_y]\text{O}_2$ ($x + y \leq 0.5$) studied by in situ high temperature XRD, *J. Electrochem. Soc.* 155 (2008) A952, <https://doi.org/10.1149/1.2988729>.
- [41] Y.K. Sun, S.T. Myung, B.C. Park, J. Prakash, I. Belharouak, K. Amine, High-energy cathode material for long-life and safe lithium batteries, *Nat. Mater.* 8 (2009) 320–324, <https://doi.org/10.1038/nmat2418>.
- [42] S.-M. Bak, E. Hu, Y. Zhou, X. Yu, S.D. Senanayake, S.-J. Cho, K.-B. Kim, K.Y. Chung, X.-Q. Yang, K.-W. Nam, Structural changes and thermal stability of charged $\text{LiNi}_x\text{Mn}_y\text{Co}_z\text{O}_2$ cathode materials studied by combined in situ time-resolved XRD and mass spectroscopy, *ACS Appl. Mater. Interfaces* 6 (24) (2014) 22594–22601, <https://doi.org/10.1021/am506712c>.
- [43] M. Hirayama, H. Tomita, K. Kubota, R. Kanno, Structure and electrode reactions of layered rocksalt LiFeO_2 nanoparticles for lithium battery cathode, *J. Power Sources* 196 (2011) 6809–6814, <https://doi.org/10.1016/j.jpowsour.2010.10.009>.
- [44] Y. Li, Y. Gao, X. Wang, X. Shen, Q. Kong, R. Yu, G. Lu, Z. Wang, L. Chen, Iron migration and oxygen oxidation during sodium extraction from NaFeO_2 , *Nano Energy* 47 (2018) 519–526, <https://doi.org/10.1016/j.nanoen.2018.03.007>.